Journal of Catalysis **194,** 385–392 (2000)
doi:10.1006/jcat.2000.2931, available online at http://www.idealibrary.com on IDEAL®

Structural Characteristics and Redox Behavior of CeO_2–ZrO_2/Al_2O_3 Supports

M. Fernández-García,[1] A. Martínez-Arias, A. Iglesias-Juez, C. Belver, A. B. Hungría, J. C. Conesa, and J. Soria

Instituto de Catálisis, CSIC, Campus Cantoblanco, 28049 Madrid, Spain
E-mail: m.fernandez@icp.csic.es

Received February 23, 2000; revised May 22, 2000; accepted May 24, 2000

Two alumina-supported Ce–Zr mixed oxide samples (with 10 and 33 wt% loads) are prepared by a microemulsion method, and their structural and redox properties are investigated using Electron Paramagnetic Resonance (EPR) and Raman spectroscopies, X-ray diffraction, temperature-programmed reduction, and transmission electron microscopy. The results show that the preparation method produces highly dispersed Ce–Zr materials which crystallize with an average particle size around 2 nm, the latter depending only weakly on the loading in the range analyzed. The Ce–Zr mixed oxide particles formed have Ce : Zr atomic ratios close to 1 with a slight enrichment in Ce for the 33 wt% CeO_2–ZrO_2/Al_2O_3 sample, and present a t″ phase type tetragonal symmetry. In both samples, EPR results show that a certain amount of the mixed oxide is present on the alumina surface as 2D (two-dimensional) patches which have redox sites with properties different from those existing in 3D, bulk-like mixed oxide particles; the characteristics of these latter also differ from those observable in unsupported Ce–Zr mixed oxide (possibly due to an epitaxial relationship with the alumina surface), as evidenced by the absence of formation of associated oxygen vacancies on the samples subjected to outgassing at 773 K. Redox cycling of these materials shows a decrease in reduction onset temperature, similar to the behavior known for unsupported Zr–Ce oxides.

I. INTRODUCTION

Alumina-supported ceria-promoted systems constitute the present state of the art for the three-way catalysts (TWCs) used for elimination of pollutants (NO_x, CO, and hydrocarbons) in automobile exhausts (1, 2). Ceria, CeO_2, and zirconia, ZrO_2, play an integral role in providing oxygen storage which broadens the conversion efficiency for all three pollutants during rich/lean perturbations associated with the feedback control regulating the air-to-fuel ratio used by the engine. Additionally, these components (Ce, Zr) favor noble metal dispersion, increase thermal stability, and promote water–gas shift, steam reforming, and CO oxidation reactions (1–3). All these effects are intimately related with the properties of the noble metal (NM)–ceria/zirconia interface, which primarily promotes oxygen activation through a route involving anion vacancies but also changes drastically the NM response to the reaction atmosphere (4–6).

At present, CeO_2–ZrO_2 mixed oxides containing TWCs constitute the most advanced technology for the development of closed coupled catalysts mounted near the exhaust ports of the engine. This setup allows reduction of hydrocarbons (HC) and CO emissions and, consequently, sharply cuts them during warm-up (7). The ceria–zirconia component enhances the classical ceria behavior by its higher oxygen storage capacity (OSC) and resistance to thermal aging, the best compromise between both beneficial effects being reached for Ce : Zr atomic ratios close to unity (8). However, the redox properties, including OSC, of Ce–Zr materials are also dependent on the geometrical structure of the mixed oxide (3). So, optimum performance under reaction conditions would correspond to mixed oxides of composition $Ce_xZr_{1-x}O_2$ (x close to 0.5) which show a pseudo-cubic t″ phase, i.e. display an X-ray diffraction pattern indexable in the cubic $Fm3m$ space group but having internally tetragonal symmetry ($P4_2/nmc$) due to oxygen displacement from ideal fluorite sites (9). On the basis of extended X-ray absorption fine structure, it has been proposed that the distortion of the oxygen sublattice could make the anions more mobile, being in the origin of the improved redox properties (10). It may be noted that, as a bulk material, the t″ phase is not thermodynamically stable at room temperature (RT) for a 1 : 1 Ce : Zr atomic ratio but is supposed to be stabilized due to a small crystallite size, thus having a behavior somehow parallel to that observed in zirconia (3). This fact points out, on the other hand, the critical role of the preparation procedure in order to reach adequate Ce–Zr materials.

The situation is more complex when the Ce–Zr component has to be supported on a high surface carrier such as alumina. The preparation of the Ce–Zr promoter in highly dispersed form, with homogeneous composition and adequate geometrical structure, is still an open matter (11).

[1] To whom correspondence should be addressed.

0021-9517/00 $35.00

On the other hand, it is well known that the redox properties of these materials may suffer notable changes from bulk to supported phases; this is indeed the case for ceria. Previous work has evidenced the presence of more reducible sites, easily producing anionic vacancies, associated with bidimensional ceria patches in contact with alumina, as well as a modification of the proportions of single and double vacancies formed in larger tridimensional ceria particles which have preferential orientations with respect to the alumina carrier due to interactions with the latter (12).

For all these reasons, it is important to devise adequate methods for preparing samples of optimally controlled structure which facilitate a clear analysis and understanding of CeO_2–ZrO_2/Al_2O_3-based systems. Here, we will study two samples of Ce–Zr mixed oxide supported on γ-alumina prepared by a microemulsion method which, in the case of bulk $CeZrO_4$, yields an homogeneous t″ material with high surface area (13). Specific attention will be paid to clarifying the nature and properties of the anionic vacancies which may be formed on these materials, as they are key elements in the redox interplay between the ceria-containing and NM components in TWCs.

II. EXPERIMENTAL

Two ceria–zirconia/alumina supports with 10 and 33 wt% content of $ZrCeO_4$ (10CZA and 33CZA; $S_{BET} = 186\ m^2\,g^{-1}$ and $S_{BET} = 164\ m^2\,g^{-1}$, respectively), were prepared using an adaptation of the microemulsion method used previously for preparing the unsupported oxide (13): a γ-Al_2O_3 powder (Condea Puralox, $S_{BET} = 180\ m^2\,g^{-1}$) is added to an inverse emulsion containing an aqueous solution of (equimolar) Zr(IV) and Ce(III) nitrates (Aldrich) dispersed in *n*-heptane using Triton X-100 (Aldrich) as surfactant and hexanol as cosurfactant. This suspension is mixed with another emulsion, similar to the first one, containing as aqueous phase an alkaline solution (tetramethylammonium hydroxide—TMAH; Aldrich). The resulting mixture, with all Ce and Zr coprecipitated, was stirred for 24 h, centrifuged, decanted, and rinsed with methanol. After drying overnight at 353 K these supports were calcined at 773 K for 2 h under dry air flow. Chemical analysis of the CZA specimens gave Zr/Ce atomic ratios of 1.0 ± 0.1. A zirconium-free 10CA reference specimen ($S_{BET} = 190\ m^2\,g^{-1}$) containing a 10 wt% content of CeO_2 supported on alumina was prepared by a similar procedure; unsupported Ce–Zr mixed oxide samples with various cation ratios, prepared also by the microemulsion method, were used as well as references for XRD and Raman experiments.

Powder X-ray diffraction (XRD) patterns were recorded on a Siemens D-500 diffractometer using nickel-filtered Cu $K\alpha$ radiation operating at 40 kV and 25 mA. Spectra were taken with a 0.025° step size and using a counting time of 1 s for reference samples and 5 s for the 10CZA and 33CZA materials.

Transmission Electron Microscopy (TEM) experiments were carried out using a JEOL 2000 FX (0.31-nm point resolution) equipped with a LINK (AN 10000) probe for energy dispersive X-ray spectroscopy (EDS) analysis. Portions of samples were crushed in an agate mortar and suspended in cyclohexene. After ultrasonic dispersion, a droplet was deposited on a copper grid supporting a perforated carbon film. Micrographs and electron diffractograms and, when necessary, dark-field images were recorded over selected areas with compositions previously characterized by EDS.

Raman spectra were obtained at room temperature (RT) with a Bruker RFS-100 FT-Raman spectrometer provided with a diode-pumped germanium solid-state detector, which operates at liquid nitrogen temperature. An NdYAG laser was used as excitation source with a power of ca. 10 mW. Powdered samples were pressed in a holder and analyzed (200 scans, 4 cm^{-1} resolution) without further treatment.

Electron paramagnetic resonance (EPR) spectra were recorded at 77 K with a Bruker ER 200 D spectrometer operating in the X-band and calibrated with a DPPH standard ($g = 2.0036$). Portions of ca. 30 mg. were placed inside a quartz probe cell with greaseless stopcocks. A conventional dynamic high-vacuum line was used for vacuum treatment at 773 K. Over this preconditioned surface, oxygen ($210\ \mu mol \cdot g^{-1}$) adsorption at 77 K, followed by 30 min warming to RT and overnight outgassing at 77 K (residual pressure 1×10^{-4} mbar), was performed (this treatment will be referred to as oxygen adsorption at RT). Experiments were continued by subsequent outgassing at RT and new recording of the EPR spectrum.

Temperature-programmed reduction–mass spectrometry (TPR–MS) experiments were carried out using portions of sample of ca. 200 mg calcined *in situ* in dry air at 773 K. A 4% H_2/Ar blend mixture with a total flow of $50\ cc \cdot min^{-1}$ regulated with mass flow controllers was used during a $10\ K \cdot min^{-1}$ ramp up to 1173 K. This was followed by an *in situ* calcination at 773 K, after which the catalysts were subjected to a second TPR. Evolved gases were analyzed by using a VG 100-D (Balzers) mass spectrometer monitoring the m/z ratios 2 (H_2), 18 (H_2O), 28 (N_2/CO), 30 (NO/NO_2), 32 (O_2), 40 (Ar), 44 (CO_2), and 46 (NO_2).

III. RESULTS AND DISCUSSION

Structure and Morphology of the Samples: XRD, Raman and TEM Experiments

Powder XRD diffraction patterns of the CZA samples are depicted in Fig. 1. These data indicate that 10CZA contains domains of supported compound oxide which are barely able to give resoluble diffraction peaks (only a

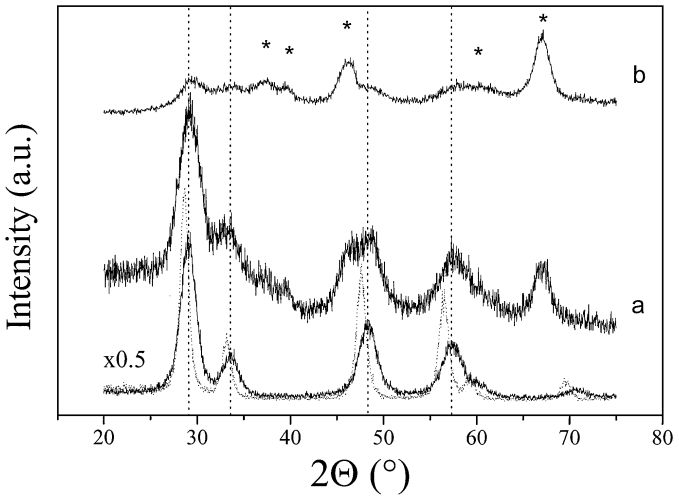

FIG. 1. XRD diffractograms of the (a) 33CZA and (b) 10CZA samples. CeO_2 (dashed line) and $Ce_{0.66}Zr_{0.33}O_4$ (full line) reference diffractograms are also included at the bottom of the figure. Alumina peaks are marked with asterisks. Vertical lines highlight peak positions for the $Ce_{0.66}Zr_{0.33}O_4$ material.

TABLE 1

XRD/TEM/ED/EDS Main Results

Sample	Cell parameter (Å)[a]	Particle size (Å)[b]	$(Zr/Ce)_{at.\ ratio}$[c]	$(Zr+Ce/Al)_{at.\ ratio}$[c]
10CZA	5.30[e]	17[f]	0.9–1.0	$0.4–1.0_5$
33CZA	5.32[d]/5.33–5.40[e]	30[d]/24[f]	0.5–1.3	0.2–2.9

[a] Fluorite-type cell with $Fm3m$ symmetry is considered.
[b] From XRD results using Scherrer formulae or from dark-field TEM images taken using the (111) and (200) ED rings of fluorite-type structures.
[c] Data from EDS. Zr + Ce/Al ratios are reported only for zones where the Zr/Ce atomic ratio is obtained with confidence. See text for details.
[d] XRD results.
[e] ED results.
[f] Dark-field TEM image results.

feature at 2θ ca. 29° is distinctly discernible, corresponding to the (111) spacing of the mixed oxide), while the 33CZA specimen presents broad but well-resolved peaks which can be conveniently indexed in the $Fm3m$ space group giving a cell parameter of 5.32 ± 0.04 Å. A complementary TEM/ED (electron diffraction) study does, however, show the existence of diffracting ceria–zirconia particles in both 10CZA and 33CZA samples (Table 1/Fig. 2). In both

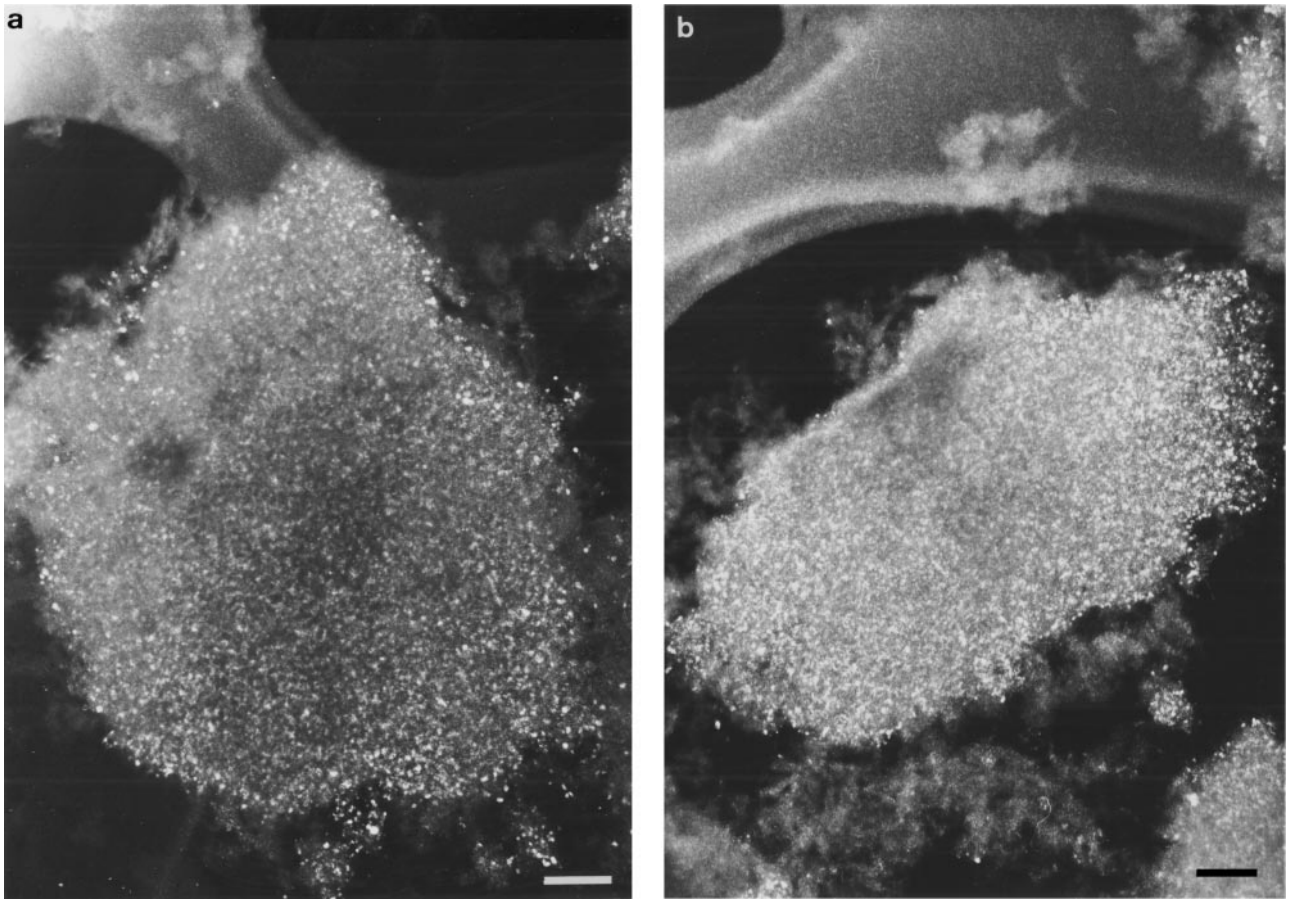

FIG. 2. Dark-field TEM images of (a) 33CZA and (b) 10CZA specimens. Both horizontal scales correspond to 50 nm.

cases, the ED features due to the Ce,Zr component can be indexed in the *Fm*3*m* space group, and they indicate for the 10CZA support a cell parameter of 5.30 ± 0.01 Å while for the 33CZA material the latter parameter takes values in the 5.33–5.40 Å interval, depending on the zone analyzed.

Considering globally the diffraction studies, and due to the linear relationship existing for Ce–Zr mixed oxides between the cell parameter and the Zr : Ce atomic ratio (1, 3), an estimation of this latter quantity can in principle be made. It must be considered, however, that, as pointed out recently (3), in high-surface Ce–Zr materials like catalysts the slope of this linear correlation is different from that reported for low-surface/ceramic oxides, limiting the accuracy of the Zr : Ce atomic ratio estimations made by using this method. Nevertheless, assuming the correlation for high-surface materials, which fits our data well for the set of bulk Ce–Zr mixed oxides prepared by microemulsion (data not shown), and considering the EDS results presented in Table 1, it can be concluded that the 10CZA sample contains a Ce–Zr mixed oxide of reasonably homogeneous composition having a Ce molar content percentage close to 50%, while the corresponding 33CZA mixed oxide has a more heterogeneous nature and presents a crystalline phase which on average, and according to the XRD data, can be described as $Ce_{0.60}Zr_{0.40}O_4$. This result implies that, in the latter sample, part of the Zr is not detected by any of the diffraction techniques and must be in a nearly amorphous form, as also occurs in CeO_2–ZrO_2/Al_2O_3 specimens prepared by coimpregnation (11). Of course, this structural description of the Ce–Zr phases formed in the CZA specimens refers only to the main characteristics of the systems; the complex nature of these supports (indeed indicated in the XRD/ED studies) does not allow us to obtain a more detailed picture.

In contrast to the XRD/ED patterns, which give information related mainly to the cation sublattice, Raman spectra of these fluorite-type oxide structures are dominated by oxygen lattice vibrations (14) and (obviously) are sensitive to the crystalline symmetry, being thus a potential tool to obtain additional structural information. While CeO_2 has only one Raman-active band (due to a vibration mode of F_{2g} symmetry) centered at 465 cm^{-1}, the oxides with crystal symmetry decreased to the tetragonal $P4_2/nmc$ space group contain six active modes of (1) A_{1g}, (3) E_{2g}, and (2) B_{1g} symmetry (15). In fact, the presence of bands at 316 and 636 cm^{-1} in Ce–Zr mixed oxides has been claimed to respond to such symmetry in a pseudo-cubic t″ phase (15). The Raman spectra shown in Fig. 3 give, therefore, evidence of the presence of the latter phase for the 33CZA sample. The 10CZA material does not show detectable Raman bands; the same happens with the 10CA reference (data not shown). This can be due to a combination of distortions/disorder of the oxygen sublattice (influenced by the sharing of O^{2-} anions with the alumina support) and

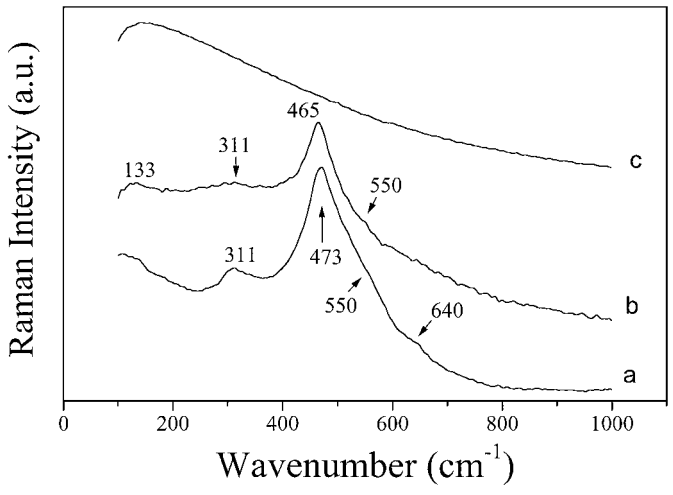

FIG. 3. Raman spectra of (a) bulk $CeZrO_4$, (b) 33CZA, and (c) 10CZA samples.

a mask effect produced by the strong fluorescence contribution coming from the alumina. Such crystalline disorder may also contribute (to a lesser extent) to the absence of well-developed peaks in the XRD spectra for this sample.

Although the Raman and XRD data give scarce information on the state of the supported oxide in 10CZA, the analysis of its ED pattern, together with the similarity in average particle size (slightly smaller for 10CZA) detected in both CZA supports (see Table 1 and compare Figs. 3a and 3b), strongly suggest that the low-loaded sample contains a mixed oxide phase similar in structure (although with lower crystallinity) to that detected in 33CZA, therefore corresponding also to the pseudo-cubic t″ phase of internal tetragonal symmetry. In this respect, it must be recalled that the stabilization at RT of this thermodynamically unstable phase for Ce molar contents below ca. 65–70% is claimed to be related to a small crystallite size (3, 9, 12), although an additional stabilization effect of the alumina carrier can not be excluded.

As commonly occurs in this type of material, the Ce–Zr mixed oxide phases formed are irregularly dispersed in the alumina support (see Zr + Ce/Al atomic ratios of Table 1). It can be noted that there are zones of the samples with practical absence of Ce and Zr; the observations from such zones are not included in the data reported in the last column of Table 1 due to the higher inaccuracy in the EDS estimation of the Ce, Zr amounts. In general, the average particle size detected by TEM is rather small, about half of that obtained by coimpregnation of Ce and Zr in the case of a 30 wt% specimen (11). This is an expected result, as the microemulsion method normally improves the dispersion of the active elements over the level achieved by classical impregnation methods. More interesting is the fact that, contrarily to the behavior detected in ceria/alumina samples prepared by impregnation (12), the more than threefold increase of the

Ce–Zr loading does not produce a large increase in the average size of the observed particles (Table 1/Fig. 2); rather, a plateau in size around 2–3 nm is reached for the Ce–Zr mixed oxide particles in the concentration range explored (10–33 wt%).

Redox Reactivity of the Dispersed Oxide: EPR and TPR Experiments

Further insight into structural characteristics and redox properties of this kind of sample can be achieved with EPR experiments using oxygen as probe molecule and examining the characteristics of superoxide radicals formed on the surface (12, 13, 16–18). Such EPR data, obtained for samples examined here, are given in Fig. 4. The determination via computer simulations (also depicted in Fig. 4) of the EPR parameters for the different overlapping signals present, and their classification and assignment to specific radical types, have been made considering previous experience on alumina-supported ceria and unsupported Zr–Ce mixed oxide samples (12, 13, 16–18). The main characteristics and relative contributions of the superoxide radicals detected are summarized in Table 2.

The spectrum obtained after oxygen adsorption at RT on sample 10CZA (Fig. 4a) is formed mainly by the overlapping of signals OCA1 and OCA2 (with an intensity ratio OCA2/OCA1 = 1.4), significantly lower contributions from signals OC1, OC2, and OZ being also required to achieve a satisfactory simulation. On the other hand, sample 33CZA, while also showing a large contribution from signal OCA1 and OCA2 (now with an intensity ratio OCA2/OCA1 = 1.2), displays relatively higher contributions from signal type OC (particularly from OC2) and OZ signals (Fig. 4b). Subsequent outgassing at RT leads to the disappearance of signals OCA1, OCA2, and OC2 for both samples (Figs. 4c and d), the spectra being formed by overlapping of signals OZ and OC1 for 10CZA and OZ, OC1, and OC3 for 33CZA (Figs. 4c and 4d). The relatively higher contribution of signal OZ, with respect to signal type OC, in the spectrum of 10CZA (compare Figs. 4c and 4d) is worth noting.

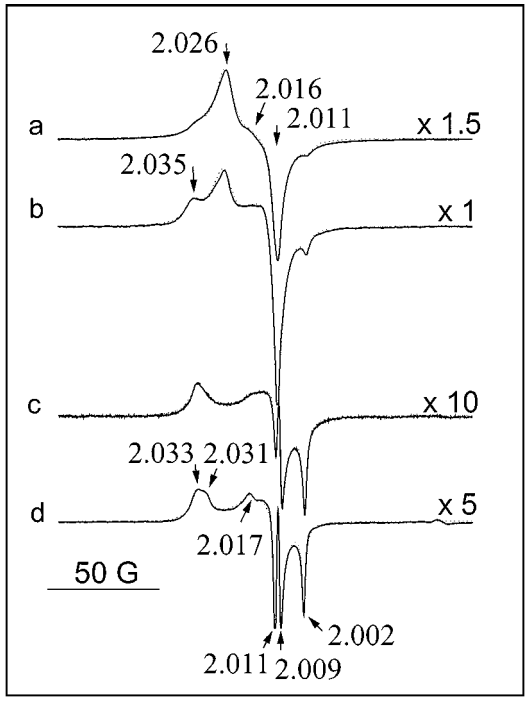

FIG. 4. EPR spectra following oxygen adsorption at RT (and elimination of excess O_2 by pumping at 77 K) on the samples outgassed at 773 K, (a) 10CZA, (b) 33CZA, and after subsequent outgassing at RT, (c) 10CZA, (d) 33CZA. Dotted lines indicate best-fit computer simulated spectra.

Signal types OC (OC1, OC2, and OC3) and OCA (OCA1 and OCA2) can both be ascribed (using formal charges) to O_2^-–Ce^{4+} species (assumed to be formed by electron transfer to O_2 from the sample surface), on the basis of their similarity to signals observed previously in oxygen adsorption experiments, using ^{17}O-enriched oxygen mixtures, on ceria-related materials (16–18). By analyzing their EPR signals, information can be obtained on the kind of reduced centers

TABLE 2

Characteristics of the EPR Signals Observed after Oxygen Adsorption at RT on the Samples Treated in Vacuum at 773 K

Signal	EPR parameters[a]	Assignment	Intensity (μmol · g_{CeZrO4}^{-1})[b]	
			10CZA	33CZA
OCA1	$g_\perp = 2.025$, $g_\parallel = 2.012$	O_2^-–Ce^{4+} formed on	4.8	2.0
OCA2	$g_z = 2.026$, $g_x = 2.016$, $g_y = 2.011$	2D entities		
OC1	$g_z = 2.033$, $g_x = 2.013$, $g_y = 2.011$	O_2^-–Ce^{4+} formed on	0.5	1.3
OC2	$g_z = 2.035$, $g_x = 2.012$, $g_y = 2.011$	isolated vacancies		
OC3	$g_z = 2.031$, $g_x = 2.017$, $g_y = 2.011$	of 3D entities		
OZ	$g_z = 2.033$, $g_y = 2.009$, $g_x = 2.002$	O_2^-–Zr^{4+}	0.4	0.5

[a] Axes attribution follows criteria of previous work (12, 13, 16, 17).

[b] Evaluated by double integration of the spectra and comparison with a copper sulfate standard, and considering computer simulation results.

generated on the sample surface by reduction treatments. In our previous experience, signals of the OCA type are observed only in alumina-supported ceria samples (12, 16), while OC-type signals are detected in unsupported ceria or Ce–Zr mixed oxide samples (13, 17, 18) and are absent in alumina-supported specimens where a very large ceria dispersion is achieved (12). The observed differences in both EPR parameters and stability against outgassing are explained by considering the different chemical environment of the cerium ions where they are formed, dispersed cerium ions belonging to 2D patches on the alumina surface (13) in the case of signals of type OCA, and cerium ions at the surface of aggregated or 3D-type entities for signals of type OC (12, 13, 16–18). One difference of the present results, when compared with previous experience, is that of signal OC2; while displaying parameters typical of O_2^-–Ce^{4+} species formed on aggregated 3D phases, it shows a relatively low stability, disappearing upon outgassing at RT as it occurs for type OCA signals. Since such behavior is observed for this type of signal only in the supported mixed oxide materials studied here, and was not found in previous investigations on unsupported ceria or Zr–Ce mixed oxide or on alumina-supported ceria (12, 13, 16–18), we can propose an assignment to oxygen radicals formed at the interface between alumina and 3D Zr–Ce mixed oxide particles.

In previous works, it was possible to classify the various O_2^-–Ce^{4+} species of OC-type formed on 3D particles (in unsupported ceria (18), Zr–Ce mixed oxide (13, 17), or relatively large ceria particles on alumina present in CeO_2/Al_2O_3 samples (12)), differentiating between radicals formed on isolated or associated oxygen vacancies. Attending to their EPR parameters, all signals of type OC observed in the present case belong to the former group. Since a significant amount of associated vacancies are formed by the outgassing treatment in unsupported $ZrCeO_4$ (13, 17), the exclusive presence of isolated vacancies suggests that the particles of mixed oxide dispersed on alumina are influenced by their growing on the carrier surface (i.e., by an epitaxial relationship), so as to affect largely the types of reduced centers that can be formed on them, and thus also their redox properties. A similar result has been recently revealed for small alumina-supported ceria particles (12).

Signal OZ, on the other hand, is attributed to O_2^-–Zr^{4+} radicals (13, 17, 19). In the case of unsupported $ZrCeO_4$ (13, 17), the relatively high amount of such radicals observed in spite of the low reducibility of zirconium cations led to the proposal of the existence of oxygen transfer phenomena by which O_2^- species formed on Ce^{3+} migrated to Zr cations and were stabilized preferentially due to their higher charge/radius ratio. A relatively large amount of this species is observed here also; such a spillover phenomenon can be therefore presumed to occur also in these alumina-supported samples. The observation of only one O_2^-–Zr^{4+} signal for both CZA specimens could then suggest that this oxygen radical is related here mainly to the 3D mixed oxide particles. In such a case, the higher OZ/OC signal intensity ratio shown by 10CZA (comparing Figs. 4c and 4d), which can not be justified on the basis of a different particle size as both samples have roughly similar 3D Ce–Zr geometrical properties (Table 1/Fig. 2), would point to a moderate enrichment in Ce of the 3D particles formed on 33CZA, in agreement with the data discussed in the previous subsection. However, the variation in the amount of OZ species when going from the 10CZA to the 33CZA sample is intermediate between those observed for the OC- and OCA-type signals; therefore, the association of the sites forming signal OZ mainly with 3D species rather than with 2D species is not straightforward.

The observation of signals of the OCA type reveals, as mentioned above, the presence on the sample surface of 2D patches (not detected by XRD nor TEM–ED) distinguishable from 3D particles of the supported (mixed) oxide. Within the former, signals OCA2 and OCA1 can be attributed to radicals formed, respectively, at the surface or at the borders of these 2D patches (12, 16); the similar ratio between the intensities of both signals indicates thus a more or less similar average size of those patches in both CZA samples. Concerning the relative amounts of 2D and 3D species, the results given in Table 2 show that, for the same amount of dispersed (Ce,Zr) oxide, the amount of superoxide radicals formed over 2D particles is 2.4 times higher in the 10CZA case. Moreover, if expressed per gram of sample, they show that the microemulsion method yields 2D entities, the amount of which increases moderately with the Ce–Zr loading (OCA signals amount to ca. 0.5 and 0.6 μmol g^{-1} for 10CZA and 33CZA, respectively), while the amount of 3D entities increases much faster (corresponding amounts of OC signals are 0.05 and 0.4 μmol g^{-1}). Thus 2D entities are present in relatively higher amounts at lower Zr–Ce loadings, in concordance with previous experience in CeO_2/Al_2O_3 samples (12). Unfortunately, since the cerium cations in such 2D entities have higher reducibility than those present at the surface of 3D particles (12, 16), it is difficult to determine in absolute terms the relative proportion of each kind. Anyway, 2D patches seem to dominate the particle size distribution for the 10CZA case, as diffraction studies do not reveal a significant contribution from 3D entities and the EPR results give evidence that the redox centers observed in this material occur mostly on 2D entities, while in the 33CZA sample 3D particles of limited size must constitute the dominant contribution since 2D entities appear in similar absolute amounts for both samples.

The EPR data do not by themselves allow us to ascertain the Zr/Ce composition of the 2D dispersed patches (which are not detected in the TEM, XRD, and Raman experiments). The shapes of the OCA signals are similar to those observed on Zr-free ceria/alumina samples, but this observation is not determinant in this respect since OC-type

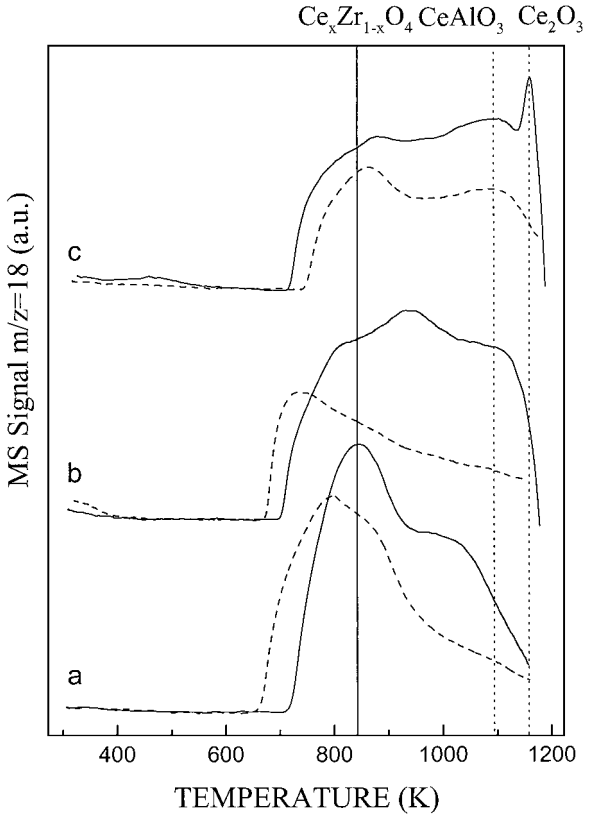

FIG. 5. TPR-MS traces of H_2O ($m/z = 18$) corresponding to (a) 33CZA, (b) 10CZA, and (c) 10CA during a first (full lines) and a second (dashed lines) temperature ramp up to 1173 K. Vertical lines correspond to characteristic reduction temperatures of bulk Ce–Zr mixed oxides (21, 22) and formation of $CeAlO_3$ and Ce_2O_3 phases (20). See text for details.

signals found on unsupported $ZrCeO_4$ are also very similar to (some of) those observed on pure ceria. However, TPR experiments have been carried out and their results, displayed in Fig. 5, shed some light on this issue.

On the first TPR run, the 10CA sample shows, after the onset of the Ce^{4+} reduction occurring at ca. 750 K, the characteristic high-temperature peaks ascribable to formation of $CeAlO_3$ (following complete reduction of small ceria particles in contact with alumina) and of Ce_2O_3 coming from the largest, bulk-like ceria entities (20). In contrast, the CZA specimens show a behavior more similar to bulk Ce–Zr mixed materials (21, 22); the peak due to formation of Ce_2O_3 is absent, and for 33CZA most of the reduction occurs in a prominent peak around 873 K, which partly shifts to higher temperatures for 10CZA, due probably to a stabilization effect induced by the interaction with the alumina surface. A further indication of the mixed oxide nature of the 2D ceria-containing entities is provided by the data obtained in a second TPR run. Sample 10CA mostly repeats the behavior displayed in the first run, except for the disappearance of the peak around 1160 K and a shift to higher temperatures of the reduction onset, the latter being probably ascribable to a higher interaction with alumina of the ceria component which has not yet formed the stable $CeAlO_3$ phase. In CZA samples, however, a significant shift of the reduction onset to lower temperatures is observed; this effect is displayed also by bulk ceria–zirconia samples, and has been attributed to partial rearrangement of the cation positions (toward an ordered structure similar to that present in pyrochlore-type Ln_2Zr2O_7 oxides) occurring during reduction at high temperatures (21, 22). The observation of this behavior also for the 10CZA sample shows clearly that the 2D entities, dominant in this specimen, have also a mixed Zr–Ce oxide character, rather than consisting of separate ceria and zirconia patches.

An additional indication of the mixed oxide character of (most of) the dispersed phase is given also by the observations concerning the formation of the $CeAlO_3$ phase. The TPR data give no clear indication of it for the CZA samples, and, accordingly, the XRD diagrams (not shown) obtained for these samples after the TRP runs of Fig. 5 display, besides the alumina support contributions, no peaks due to that $CeAlO_3$ phase, but only features attributable to a $Ce_{0.55}Zr_{0.45}O_4$ phase (i.e., containing, within the experimental error, the same at% of Ce as the initial, calcined material); this contrasts with the behavior of the 10CA sample, which does show sharp peaks of $CeAlO_3$ in the diffractogram after being subjected to the same TPR treatment. These differences further support the conclusions about the mixed oxide nature of the 2D dispersed entities present in these samples.

IV. CONCLUSIONS

The microemulsion procedure is shown to be a satisfactory method to prepare ceria–zirconia mixed oxides with Zr : Ce ratio close to 1.0, highly dispersed in an alumina carrier, with a moderately uniform particle size (in the range of a few nm) for both loadings analyzed (10 and 33 wt%). Both samples studied show 2D and 3D mixed oxide entities; the 33CZA specimen mainly contains 3D particles, somewhat enriched in Ce, while a dominant amount of 2D entities is present in 10CZA, its minority 3D particles showing a Zr/Ce ratio closer to 1. A minor amorphous (i.e., not detected by diffraction techniques) Zr-enriched phase could be present also at the carrier surface of the sample with higher loading. Overall, an average Ce content of 50 to 60 at% is detected in the three-dimensional binary oxide particles formed, having the structure of a pseudo-cubic t″ phase with internal tetragonal symmetry. The composition of the 2D entities cannot be evaluated quantitatively, but they are clearly of a mixed oxide type as evidenced by TPR and subsequent XRD data, which give results different from those obtained with a Zr-free sample.

As evidenced by the oxygen adsorption experiments followed by EPR, these specimens have redox properties

modified from those of unsupported ceria–zirconia materials: similar to the previously observed case of alumina-supported ceria, the small, 2D ceria–zirconia entities have redox characteristics that are strongly perturbed by the alumina support, while 3D particles differ from the bulk materials in being unable to form associated vacancy centers under the experimental conditions used.

ACKNOWLEDGMENTS

M.F.-G. and A.M-A. gratefully acknowledge the Ministerio de Educación of Spain and the Comunidad de Madrid for a postdoctoral contract and grant, respectively. A.I.-J. thanks the Comunidad de Madrid for a predoctoral grant. Thanks are also given to F. Sanchez and L. N. Salamanca for the EPR and TEM experiments. Support from CAICYT (Project No. MAT 97-0696-CO2-O1) and CAM (Project No. 06M/084/96) is fully appreciated.

REFERENCES

1. Trovarelli, A., *Catal. Rev. Sci. Eng.* **38**, 439 (1996).
2. Farrauto, R. J.,and Heck, R. M., *Catal. Today* **51**, 351 (1999).
3. Kaspar, J., Fornasiero, P., and Graziani, M., *Catal. Today* **50**, 285 (1999).
4. Martínez-Arias, A., Fernández-García, Conesa, J. C., and Soria, J., *J. Catal.* **182**, 367 (1999).
5. Fernández-García, M., Martínez-Arias, A., Salamanca, N. L., Coronado, J. M., Anderson, J. A., Conesa, J. C., and Soria, J., *J. Catal.* **187**, 474 (1999).
6. Martínez-Arias, A., Coronado, J. M., Cataluña, R., Conesa, J. C., and Soria, J., *J. Phys. Chem. B* **102**, 4357 (1998).
7. Hu, Z., and Heck, R. M., SAE 950254, 1995.
8. Cuif, J. P., Blanchard, G., Touret, O., Seigneurin, A., Marczi, M., and Quémere, E., SAE 970463, 1997.
9. Vlaic, G., Di Monte, R., Fornasiero, P., Fonda, E., Kaspar, J., and Graziani, M., *J. Catal.* **182**, 378 (1999).
10. Vlaic, G., Fornasiero, P., Geremia, S., Kaspar, J., and Graziani, M., *J. Catal.* **168**, 386 (1997).
11. Yao, M. H., Blaird, N. J., and Kunz, F. W., *J. Catal.* **166**, 67 (1997).
12. Martínez-Arias, A., Fernández-García, M., Salamanca, L. N., Conesa, J. C., and Soria, J., *J. Phys. Chem. B* **104**, 4038 (2000).
13. Martínez-Arias, A., Fernández-García, M., Ballesteros, V., Salamanca, L. N., Otero, C., Conesa, J. C., and Soria, J., *Langmuir* **15**, 4796 (1999).
14. Ferraro, J. R., and Nakamoto, K., "Introductory Raman Spectroscopy." Academic Press, New York, 1994.
15. Yashima, M., Arashi, H., Kakihana, M., and Yoshimura, M., *J. Am. Ceram. Soc.* **77**, 1067 (1994).
16. Soria, J., Coronado, J. M., and Conesa, J. C., *J. Chem. Soc. Faraday Trans.* **92**, 1619 (1996).
17. Martínez-Arias, A., Fernández-García, M., Belver, C., and Conesa, J. C., *Catal. Lett.* **65**, 197 (2000).
18. Soria, J., Martínez-Arias, A., and Conesa, J. C., *J. Chem. Soc. Faraday Trans.* **91**, 1669 (1995).
19. Anpo, M., Che, M., Fubini, B., Garrone, E., Giamello, E., and Paganini, M. C., *Topics Catal.* **8**, 189 (1999).
20. Shyu, J. Z., Weber, W. H., and Gandhi, H. S., *J. Phys. Chem.* **92**, 4964 (1988).
21. Baker, R. T., Bernal, S., Blanco, G., Cordón, A. M., Pintado, J. M., Rodríguez-Izquierdo, J. M., Fally, F., and Perrichon, V., *Chem. Commun.*, 149 (1999).
22. Fornasiero, P., Kaspar, J., and Graziani, M., *Appl. Catal. B.* **22**, L11 (1999).